nature communications



Article

https://doi.org/10.1038/s41467-025-58114-9

Unsaturation degree of Fe single atom site manipulates polysulfide behavior in sodium-sulfur batteries

Received: 9 July 2024

Accepted: 10 March 2025

Published online: 21 March 2025



Wanqing Song^{1,2}, Zhenzhuang Wen¹, Xin Wang¹, Kunyan Qian¹, Tao Zhang¹, Haozhi Wang ⊕ ^{1,3}, Jia Ding ⊕ ^{1,2,4} ⊗ Wenbin Hu ⊕ ^{1,2,4}

Sodium | |sulfur batteries hold great promise for grid-scale energy storage, yet their performance is hindered by the shuttling and sluggish redox of sulfur species. Herein, we report a strategic design of sulfur hosts modified with coordinatively unsaturated iron single-atom (Fe-N_r) for sodium | |sulfur batteries. Utilizing theoretical calculations, geometric descriptor γ (l_{Na-S}/l_{Fe-N}) and electronic descriptor φ ($e_{\rm g}/t_{\rm 2g}$) simultaneously correlated with the unsaturation degree of Fe- N_x site are proposed. A negative correlation between y and the adsorption strength of sodium polysulfides, along with a positive correlation between φ and the decomposition capability of Na₂S are established. The Fe-N₁ sites, with the minimum γ and maximum φ values, are identified as the optimal functional species for optimizing polysulfides behaviors. Sodium | |sulfur batteries utilizing Fe-N₁/S positive electrodes deliver improved sulfur utilization (81.4% at 167.5 mA g⁻¹), sustained rate performance $(1003.0 \text{ mAh g}^{-1} \text{ at } 1675 \text{ mA g}^{-1})$, and stable cycling $(83.5\% \text{ retention over } 450 \text{ mAh g}^{-1})$ cycles at 3350 mA g⁻¹). Moreover, Fe–N₁/S positive electrodes enable sodium | | sulfur pouch cells to deliver a sulfur utilization of 77.4% (1296.9 mAh g⁻¹) at 0.1 A g⁻¹. Our work offers a strategy for designing high-activity, fast redox sulfur positive electrodes and validates the practical potential of sodium | | sulfur batteries.

Reliable and cost-effective energy is essential for modern society's security and economic well-being, with batteries serving as a key enabler for decarbonization within the global energy sector^{1–3}. The high specific capacity (1675 mAh g⁻¹) brought by the two-electron transfer of sulfur makes room-temperature sodium||sulfur (Na||S) batteries composed of low-cost and environmentally friendly sodium metal and elemental sulfur exhibit tremendous potential in the field of large-scale energy storage^{4–6}. Na||S battery systems offer a viable pathway to achieving sustainable development goals in energy storage. However, the poor electrical conductivity of sulfur ($5 \times 10^{-28} \, \text{S m}^{-1}$

at 25 °C) and its discharge products significantly limit the kinetics of conversion reactions, leading to low sulfur utilization and rapid capacity decay due to the accumulation of inert discharge products in the electrode^{7–9}. In addition, the shuttle effect of sodium polysulfides (NaPSs) in the electrolyte leads to detrimental sulfur species loss and capacity degradation 10,11 . To cope with these challenges, the development of host materials with excellent functionality to fully exploit the potential of sulfur is important.

Carbons are widely used as host materials for active sulfur to improve the electronic conductivity of sulfur positive electrodes.

¹School of Materials Science and Engineering, Tianjin Key Laboratory of Composite and Functional Materials, Key Laboratory of Advanced Ceramics and Machining Technology (Ministry of Education), Tianjin University, Tianjin, China. ²State Key Laboratory of Precious Metal Functional Materials, Tianjin University, Tianjin, China. ³School of Materials Science and Engineering, Hainan University, Haikou, China. ⁴National Industry-Education Platform of Energy Storage, Tianjin University, Tianjin, China. ⊠e-mail: jiading@tju.edu.cn

However, weak interactions between NaPSs and non-polar carbon surfaces inevitably fail to address the poor redox kinetics of sulfur species¹²⁻¹⁴. Sulfur fixation using chemical interactions between host and sulfur species is another strategy for sulfur host design. For instance, sulfated polyacrylonitrile (SPAN) relies on the covalent bonds formed between elemental sulfur and carbon, which plays a key role in both inhibiting the shuttling of NaPSs and preventing sulfur agglomeration^{15,16}. In addition, the introduction of appropriate adsorption and catalytic sites, such as metal compounds into the carbon-based sulfur host is also one of the major strategies^{17–20}. Sulfur species are efficaciously adsorbed and rapidly converted since the polar interactions between the sites and NaPSs. Due to the severe spatial distribution mismatch between the limited adsorption/catalytic sites and the widely spread sulfur species, it is prone to the accumulation of electrochemically inert solid-phase products, the poisoning of sites and the rapid failure of the Na||S batteries^{21,22}. Therefore, constructing carbon-based sulfur hosts with atomically uniformly distributed and highly exposed single-atom sites modification is the key to enhancing the kinetics and stability of sulfur positive electrodes.

In recent years, there are pioneering works on metal single-atom (M-N₄) modified carbon materials as sulfur hosts in Na||S batteries reporting improved sulfur redox electrocatalytic activity²³⁻²⁵. Fe-N₄ sites, for example, exhibit notable catalytic activity in metal||sulfur batteries $^{26-29}$, which is closely related to the unique d-band electrons of Fe. Nevertheless, sites with such fully coordinated configurations are probably mediocre for the adsorption and catalytic conversion of NaPSs, as the symmetrical nitrogen ligands in the first coordination shells leave weakly polarized central metal atoms. Aiming to further enhance the interactions with polysulfides, single-atom sites with asymmetric coordination configurations gradually arise researchers' interests^{30,31}. The design of single-atom sites for their functionalities in Na||S electrochemistry requires careful consideration of their anchoring and converting capabilities toward NaPSs. This necessitates a systematic approach to rationally designing both the geometric and electronic structures of these sites. Moreover, given the unique characteristics of metall|sulfur systems compared to conventional electrocatalytic systems, it is imperative to identify universal descriptors for geometric/electronic structures of single-atom sites and establish the mapping between them and NaPSs behaviors to guide the design and construction of high-efficiency single-atom sites-based host materials in the Na||S batteries.

In this work, we delve into the pivotal influence of unsaturation degrees of Fe single-atom sites (Fe– N_x) on the behaviors of NaPSs. Based on theoretical calculations, two key descriptors of γ (l_{Na-S}/l_{Fe-N}) for geometric structure and φ ($e_{\rm g}/t_{\rm 2g}$) for electronic structure are developed innovatively for analyzing the unsaturation degree of Fe-N_x sites. A negative correlation is established between γ and adsorption strength of NaPSs, and a positive correlation is found between φ and the catalyzing capability of Na₂S decomposition. Accordingly, Fe-N₁ with minimum γ and maximum φ values is considered as the optimal functional species for enhancing NaPSs behaviors through theoretical screening. NallS batteries using positive electrodes with Fe-N₁ sites modification exhibit elevated sulfur utilization (81.4% at 167.5 mA g⁻¹), notable rate performance (1003.0 mAh g⁻¹ at 1675 mA g⁻¹), and stable cycling performance. When incorporated into pouch cells, the Fe-N₁based positive electrode maintains an impressive sulfur utilization rate of 77.4%, highlighting its promising potential for practical applications. These findings offer insights into the role of unsaturated single-atom sites in boosting the Na||S electrochemistry.

Results and discussion

Systematic experimental screening revealed that Fe single atoms exhibit improved performance in facilitating polysulfide conversion compared to other investigated elements (Supplementary Figs. 1 and 2). Therefore, herein Fe was chosen as active metal element for single-atom

site design in Na||S batteries. To investigate the impact of coordination unsaturation degrees for single-atom sites interacting with NaPSs, we conducted density-functional theory (DFT) calculations on Fe singleatom sites with varying nitrogen coordination number (Fe-N_x, x = 1-4) (Supplementary Fig. 3 and Supplementary Data 1). Mitigating the detrimental shuttle effect of soluble NaPSs is vital for sulfur utilization and cycling stability in Na||S batteries^{32,33}. Therefore, the adsorption strength of Fe-N_x sites with NaPSs stands as a important factor in sulfur host design. As the stoichiometric mid-point of NaPSs and the end member of the long-chain polysulfides in the reduction pathway, the effective anchoring of Na₂S₄ is particularly critical. Figure 1a delineates the configurations of Na₂S₄ adsorbed on Fe-N_x sites. Under polar interactions, the distances between central Fe atoms and ligand N atoms in several configurations stretch by different degrees (Supplementary Table 1 and Supplementary Data 1). We innovatively develop the geometric structure descriptor γ ($\gamma = l_{Na-S}/l_{Fe-N}$), where l_{Fe-N} represents the distance between Fe and N atoms directly anchored to NaPSs, and l_{Na-S} denotes the corresponding distance between Na and S atoms in NaPSs anchored by Fe and N. Theoretical calculations unveil a strong correlation between y and the binding energy of Na₂S₄ on Fe-N_x sites with varying unsaturation degrees. As depicted in Fig. 1b, the y value steadily decreases from 1.527 (Fe- N_4 - Na_2S_4) to 0.824 (Fe- N_1 - Na_2S_4) as unsaturation degree increases, while the adsorption energy for Na₂S₄ increases from $-1.467\,\text{eV}$ (Fe-N₄-Na₂S₄) to $-7.532\,\text{eV}$ (Fe-N₁-Na₂S₄). Similar relationships between binding energies and γ are also observed for Fe-N_x sites interacting with long-chain (Na₂S₈/Na₂S₆) and shortchain NaPSs (Na₂S₂/Na₂S) (Supplementary Fig. 4, Supplementary Table 2, and Supplementary Data 1), indicating that γ provides good universality in describing the adsorption of NaPSs on single-atom sites. In Fe– N_x sites with low unsaturation degrees (e.g. Fe– N_3 , Fe– N_4), fixed Fe-N bond lengths cause the adsorbed NaPSs molecules to suffer from the steric-hindrance effect of the full coordination configurations, preventing strong adsorption. Notably, the highly coordinatively unsaturated Fe-N₁ configuration allows for ample space for NaPSs adsorption, circumventing the steric-hindrance effect. In addition, the distance between the central Fe single atom and the highly unsaturated ligand N atoms can be adjusted to accommodate the NaPSs configurations for the strongest adsorption.

Moreover, addressing the high energy barrier of Na₂S oxidation is essential for improving the efficiency and stability of Na||S batteries. Based on the configuration demonstrated in Supplementary Fig. 3, Fe- N_x can be approximated as a D4h crystal field, where the 3d orbital of the central Fe atom is split into t_{2g} orbitals (d_{xy}, d_{yz}, d_{zx}) and e_g orbitals (d_{x2-y2}, d_{z2}) . Upon interaction with Na₂S, the d orbitals of Fe at the Fe- N_x site hybridize with the p orbitals of S in Na₂S (Fig. 1c), forming σ/σ^* bonds with high-energy splitting and relatively weak π/π^* bonds^{19,34}. The bonding orbitals are fully occupied after hybridization depending on the intrinsic electronic structure of Fe and S. Consequently, the low occupancy of π^* is advantageous for coupling of Na₂S and accommodating the electrons released from its decomposition, which implies a higher number of e_{g} and a lower number of t_{2g} orbital electrons. Therefore, we propose φ ($\varphi = e_g/t_{2g}$) as a proper descriptor to characterize the correlation between electronic structures of Fe-N_x and the catalytic property. From the projected density of states (PDOS) for $e_{\rm g}$ and $t_{\rm 2g}$ orbitals of Fe (Fig. 1d), φ decreases progressively with the increasing unsaturation of Fe-N_x sites. To delve deeper into the influence of unsaturation degrees for Fe-N_x sites on Na₂S decomposition, we conducted a projected crystal orbital Hamiltonian population (pCOHP) analysis. As illustrated in Fig. 1e, increasing the unsaturation of Fe-N_x sites shifts the bonding orbitals of Na-S bonds in adsorbed Na₂S molecules above the Fermi level, reducing the Na-S bond dissociation barrier. The parameter φ , describing the relationship between the catalytic activity of Fe-N_x sites and their local electronic structure, shows a positive correlation with integrated COHP (ICOHP) (Fig. 1f). Fe– N_x sites with high φ values facilitate the coupling with Na₂S

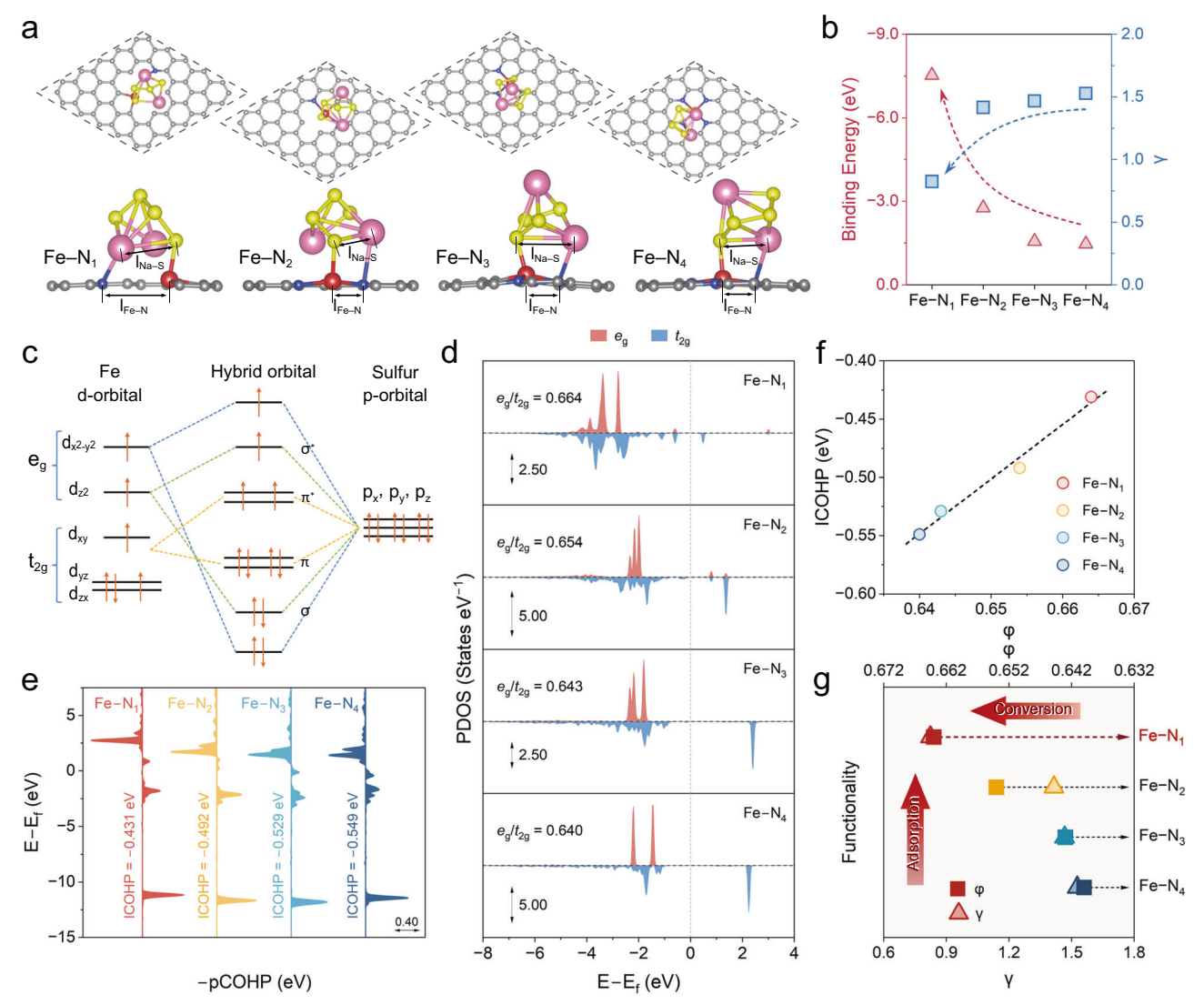


Fig. 1 | **Effects of the geometric and electronic structures of Fe-N**_x **on the behaviors of polysulfides. a** Configurations of Na₂S₄ adsorbed on Fe-N_x, in which the pink, yellow, red, blue, and grey spheres represent Na, S, Fe, N, and C atoms, respectively. **b** Relationships among unsaturation degrees of Fe-N_x, binding energies, and geometric structure descriptors (γ , $\gamma = l_{\text{Na-S}}/l_{\text{Fe-N}}$). **c** Schematic for the d-p orbital hybridization between Fe-N_x and sulfur species. **d** Projected DOS of different orbitals for Fe-N_x. **e** Projected crystal orbital Hamilton population

(pCOHP) diagrams of Na–S bonds in Na₂S adsorbed on Fe–N_x. **f** Relationship between ICOHP values of Na–S bonds in Na₂S and electronic structure descriptor $(\varphi, \varphi = e_g/t_{2g})$. **g** Schematic illustration of Fe–N_x with high unsaturation degrees for efficient sulfur redox in Na||S batteries based on geometrical/electronic structure descriptors. The atomic coordinates of the configurations are provided as a Supplementary Data 1 file, and source data are provided as a Source Data file.

molecules and adsorption of electrons released during Na₂S decomposition, thereby delivering the advantage for effective Na₂S decomposition. The electrons of NaPSs are easier to enter the bonding orbitals of Fe–N_x sites with lower φ , which brings about stronger interactions between the central Fe atoms and NaPSs. This enhanced interaction, shown by increased ICOHP, suggests that Na₂S dissociates more readily on highly unsaturated Fe–N_x sites, especially Fe–N₁ sites. The positive correlation between the descriptor φ and ICOHP permits the improved kinetics of Na₂S decomposition by modulating the orbital occupations of Fe–N_x sites.

Overall, the constructed geometric and electronic structure descriptors reveal that the unsaturation of Fe–N $_x$ sites can modulate both γ and φ . The descriptors and their functionality are illustrated in Fig. 1g. Based on the established negative correlation between γ and NaPSs adsorption strength, and the positive correlation between φ and Na₂S decomposition capability, the Fe–N₁ site stands out with the minimum γ and maximum φ values. These optimized geometry

structures circumvent the steric-hindrance effects, resulting in the strongest NaPSs adsorption. Meanwhile, the refined electronic structures provide sufficient electronic orbitals to the highest catalyzing capacity for Na₂S dissociation. Consequently, incorporating Fe–N₁ sites as functional components in sulfur hosts is the rational design.

Guided by the theoretical calculations, we synthesized sulfur hosts with Fe-N_x sites. Nitrogen-containing carbon precursors typically decompose and derivatize into carbon upon high-temperature treatment. During this process, highly reactive nitrogen species are highly susceptible to escape from the material, leaving defects in the derived carbon materials³⁵. Based on this pyrolysis-induced nitrogen escape strategy, we constructed carbon-supported Fe single atoms materials with different coordination environments. Specifically, the Fe-doped precursors (Fe-ZIF-8) were pyrolyzed at 1100, 900, and 700 °C, yielding a set of carbon host specimens possessing Fe-N_x sites (abbreviated as Fe-N_x). To determine the functionality of Fe-N_x sites,

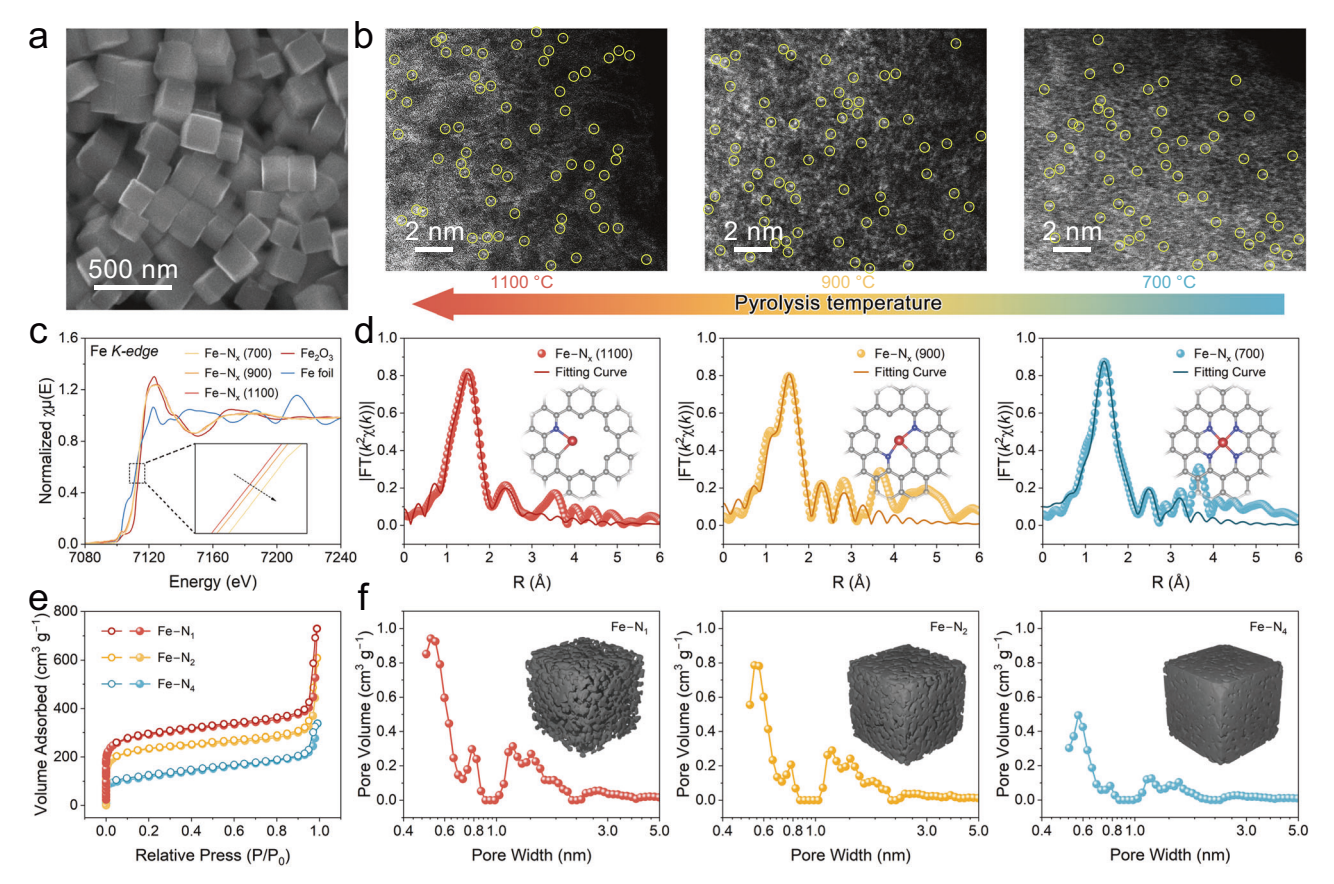


Fig. 2 | Morphology and structure characterizations of Fe- N_x host materials. a SEM image of Fe- N_x (1100). b HAADF-STEM images of Fe- N_x , with atomically dispersed iron species highlighted by yellow circles. c XANES spectra of Fe K-edge for Fe- N_x , Fe₂O₃, and Fe foil references. d EXAFS spectra and fitting curves of Fe- N_x . Insets are the fitting models in which the red, blue, and grey spheres represent Fe,

N, and C atoms, respectively. **e**, **f** N₂ adsorption–desorption isotherms (**e**) and corresponding pore size distributions (**f**) of Fe–N₁, Fe–N₂, and Fe–N₄ (Inset: Schematic illustrations of the pore structure of Fe–N_x host materials corresponding to **f**). Source data are provided as a Source Data file.

we also pyrolyzed Fe-free ZIF-8 precursors at 700 °C to obtain pure nitrogen-doped carbon (NC).

 ${\rm Fe-N_x}$ and NC specimens exhibit cubic morphologies -200 nm in size (Fig. 2a and Supplementary Fig. 5). Aberration-corrected high-angle annular dark-field scanning transmission electron microscopy (HAADF-STEM) images (Fig. 2b) reveal high densities of isolated distributions of bright dots (highlighted in yellow circles) on the surfaces of ${\rm Fe-N_x}$, originating from atomically homogeneous dispersion of Fe species. This is corroborated by energy dispersive spectroscopy (EDS) mapping images (Supplementary Fig. 5) with the uniform Fe distribution and X-ray diffraction (XRD) patterns (Supplementary Fig. 6) with amorphous features.

The local electronic structure and coordination environment of Fe single atoms obtained at different pyrolysis temperatures were studied using synchrotron X-ray absorption spectroscopy (XAS). The X-ray absorption near-edge structures (XANES) (Fig. 2c) reveal that the average valence state of Fe in Fe–N $_{x}$ ranges between 0 and +3, with a gradual decrease in valence state as pyrolysis temperature increases. This suggests a reduction in the number of ligand N atoms competing for electrons with central Fe atoms. This observation is consistent with the high-resolution Fe 2p X-ray photoelectron spectroscopy (XPS) spectra (Supplementary Fig. 7), where the peaks shift toward low binding energies with higher pyrolysis temperatures. In the Fourier-transformed extended X-ray absorption fine structure (EXAFS) spectra (Supplementary Fig. 8), all samples exhibit a main peak near ~1.47 Å, corresponding to Fe–N path 36 . The absence of peaks corresponding to the Fe–Fe bonds (2.18 Å) further confirms the effective dispersion of Fe

atoms in Fe-N $_x^{27}$. According to the *R*-space fitting results of EXAFS (Fig. 2d and Supplementary Table 3), the fitting curves strictly match the experimental data. Based on precisely determined coordination numbers (CN) of Fe-N paths, the Fe-N $_x$ specimens pyrolyzed at 700, 900, and 1100 °C are named Fe-N $_4$, Fe-N $_2$, and Fe-N $_1$, respectively. The atomic configuration analyses verified the controlled synthesis of unsaturated Fe-N $_x$ sites utilizing the nitrogen-escape strategy.

Furthermore, the variation in pyrolysis temperature significantly impacts the pore structure of Fe–N $_x$, which is crucial for constructing sulfur storage space in the host materials. As revealed in Fig. 2e, f, and Supplementary Fig. 9, the micropore volume significantly increases with rising pyrolysis temperature from 700 to 1100 °C. This phenomenon could be ascribed to the elevated pyrolysis temperature, which intensifies the volatilization of non-carbon elements during pyrolysis (Supplementary Fig. 10). Fe–N $_1$ exhibits abundant micropores and a large surface area (Supplementary Table 4), facilitating the active sites exposure and sulfur species storage.

Using the aforementioned hosts, Fe– N_x /S, and NC/S composites were prepared via the sulfur melt-diffusion method. The samples maintained the same morphology as the pristine hosts (Supplementary Fig. 11) with no residual sulfur particles observed on the surface. The XRD patterns of these composite materials (Supplementary Fig. 12) exhibited similar diffraction peaks of orthorhombic sulfur (JCPDS No. 08-0247). According to the nitrogen adsorption-desorption isotherm analysis (Supplementary Fig. 13), the micropore volumes and specific surface areas of the composites significantly decreased compared to those of the pristine hosts, indicating effective

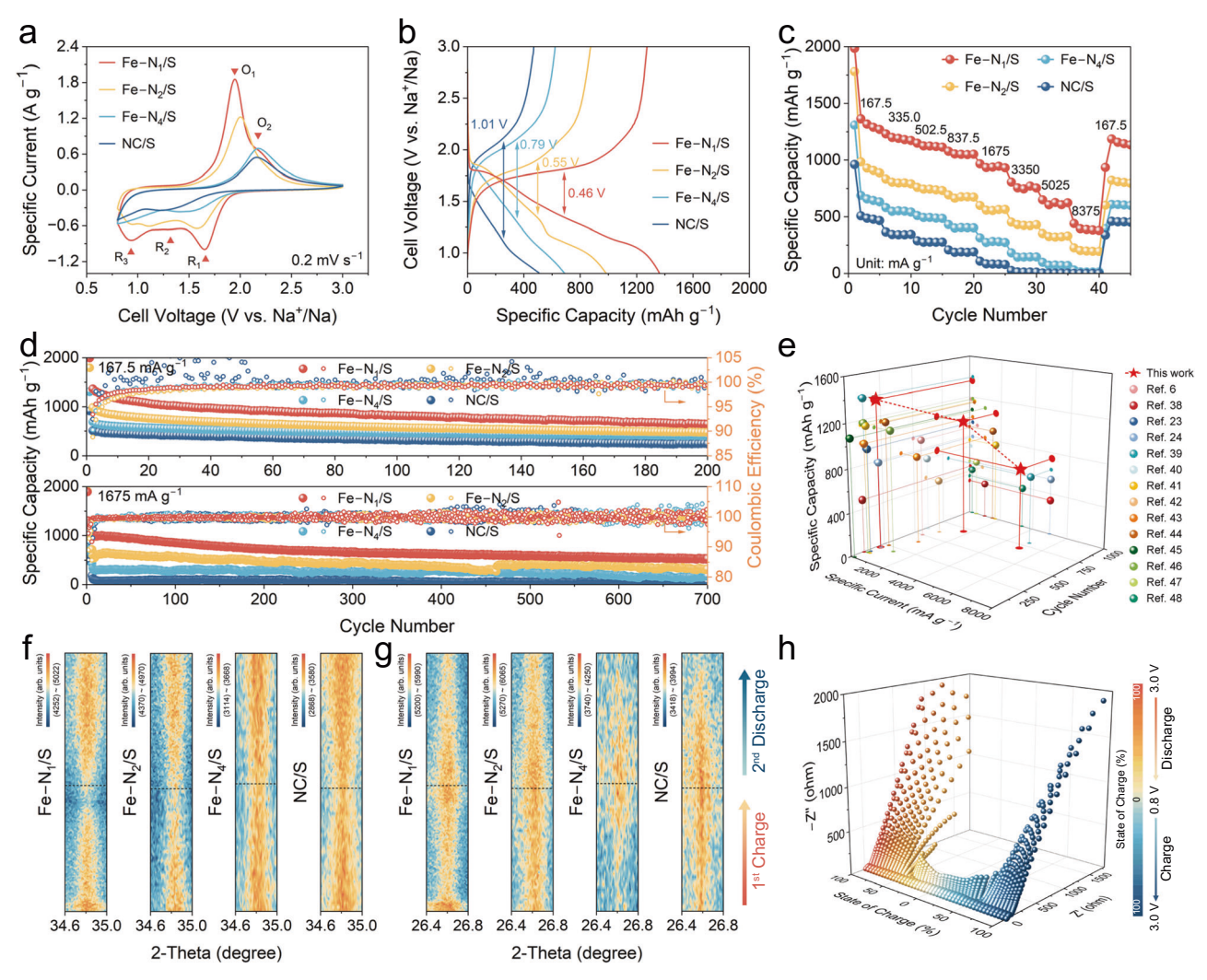


Fig. 3 | The influence of unsaturation degree in Fe-N $_x$ on electrochemical performances and sulfur redox mechanisms. a–c CV curves at 0.2 mV s⁻¹ (a), GCD profiles at 167.5 mA g⁻¹ (b), and rate performance (c). d Cycling performance of Na|| S batteries with Fe-N $_1$ /S, Fe-N $_2$ /S, Fe-N $_4$ /S, and NC/S positive electrodes. e Comparison of sulfur utilization, rate, and cycling performances of Fe-N $_1$ /S

positive electrode with the state-of-the-art positive electrodes for Na||S batteries reported. ${\bf f}$ and ${\bf g}$ In situ XRD patterns with selected ranges for Na₂S (${\bf f}$) and Na₂S₅ (${\bf g}$) of Fe-N₁/S, Fe-N₂/S, Fe-N₄/S, and NC/S positive electrodes during the 1st charge and 2nd discharge processes. ${\bf h}$ In situ EIS spectra for Na||S battery with Fe-N₁/S positive electrode. Source data are provided as a Source Data file.

sulfur encapsulation within the hosts' micropores. Resultantly, Fe–N_x/S and NC/S showed similar sulfur loadings (Supplementary Fig. 14). XPS spectra depicted the interactions between sulfur species and the hosts. Due to the strong electronegative sulfur, the high-resolution Fe 2p XPS spectra in Fe–N_x/S shifted toward higher binding energies (Supplementary Fig. 15), while S 2p XPS spectra shifted in the opposite direction³⁷. This change is more pronounced in the highly unsaturated Fe–N₁/S, which adequately demonstrates the strong propensity of the interaction between S and Fe–N₁ sites.

To understand the sulfur redox in Fe–N_x/S and NC/S positive electrodes, cyclic voltammetry (CV) measurements were conducted. As shown in Fig. 3a, the Fe–N₁/S positive electrode exhibits three reduction peaks at 1.653 V (R₁), 1.299 V (R₂), and 0.941 V (R₃), and two oxidation peaks at 1.947 V (O₁) and 2.182 V (O₂). The CV curve of the Fe–N₂/S positive electrode resembled that of the Fe–N₁/S positive electrode, albeit with a lower response current and larger polarization. In contrast, Fe–N₄/S and NC/S positive electrodes exhibit severe polarization, resulting in weak reduction peaks and a single oxidation peak within the voltage range of 0.8–3.0 V. This phenomenon indicates that unsaturated Fe–N₁ sites could facilitate the kinetics of sulfur redox.

Figure 3b shows the galvanostatic charge-discharge (GCD) profiles of these four positive electrodes at 167.5 mA g⁻¹ for the 2nd cycle. The Fe-N₁/S positive electrode exhibits a discharge-specific capacity of 1363 mAh g⁻¹, corresponding to a sulfur utilization of 81.4%. The respective sulfur utilization for Fe-N₂/S, Fe-N₄/S, and NC/S positive electrodes are 58.8%, 41.1%, and 30.3%, underscoring the benefits of Fe-N_x sites with high unsaturation degrees in enhancing sulfur electrochemical activity. Fe-N₁/S electrodes with a high sulfur content of ~60% and 70% delivered slightly lower capacities of 1228 and 1137 mAh g⁻¹ (Supplementary Figs. 16, 17), which are still higher than most previously reported positive electrodes with comparable sulfur content (Supplementary Table 5). The Fe-N₁/S positive electrode delivers the lowest polarization voltage (0.46 V), representing efficient sulfur redox and Na⁺ diffusion. Of note, the capacity contribution from the pure hosts is minimal (Supplementary Fig. 18), confirming that the positive electrode capacity arises from reversible sulfur redox.

In terms of rate performance (Fig. 3c), the Fe–N₁/S positive electrode achieved specific capacities of 760.1, 615.7, and 388.5 mAh g⁻¹ at 3350, 5025, and 8375 mA g⁻¹, respectively, surpassing those of other three positive electrodes. Furthermore, upon reverting to 167.5 mA g⁻¹,

the battery-specific capacity recovered to 1167.6 mAh g⁻¹ (93.4% of the specific capacity at the 5th cycle), underscoring that batteries using the Fe-N₁/S positive electrode exhibit robust reversibility. The GCD curves of Na||S batteries with the Fe-N₁/S positive electrode (Supplementary Fig. 19) signify clear and analogous discharge slopes and charge plateaus at various specific currents, with minimal voltage hysteresis. Resultantly, Fe-N₁ sites demonstrate notable rate performance and rapid kinetics for sulfur species conversions. In order to strictly prove that the enhanced sodium||sulfur electrochemistry essentially stemmed from Fe-N_x catalytic sites instead of other physical factors, Fe-free NC hosts were also investigated. As shown in Supplementary Fig. 20, each NC host exhibits a similar surface area as the counterpart Fe-N_x host synthesized at the same temperature, yet leading to much lower sulfur utilization and rate capacities (Supplementary Fig. 21). Also, the Fe– N_x and Fe-free NC hosts synthesized at the same temperature have similar electronic conductivities yet leading into significantly different Na||S electrochemistry (Supplementary Table 6). These control groups eliminated the effects of surface area and electronic conductivity in electrochemical performance improvement.

Figure 3d illustrates the cyclic performances of different positive electrodes at 167.5 and 1675 mA g⁻¹. At 167.5 mA g⁻¹, the reversible capacities of Fe-N₂/S, Fe-N₄/S, and NC/S positive electrodes were 475.2, 398.6, and 241.8 mAh g⁻¹ after 200 cycles, respectively. By contrast, the Fe-N₁/S positive electrode maintained a high reversible specific capacity of 647.8 mAh g⁻¹ and impressive Coulombic efficiency of 99.4% after 200 cycles, showcasing the evident electrocatalytic capability of Fe-N₁ sites for NaPSs redox. Further investigation into the long-term stability of each positive electrode was conducted at a high specific current of 1675 mA g⁻¹. Among them, the Fe–N_I/S positive electrode demonstrated a substantial reversible specific capacity of 1003 mAh g⁻¹ and stably operated for 700 cycles. At 3350 mA g⁻¹, the Fe–N₁/S positive electrode delivered negligible capacity loss over 300 cycles and 83.5% capacity retention after 450 cycles (Supplementary Fig. 22). It is instructive to compare the Fe-N₁/S positive electrode assembled Na||S battery with the reported state-of-the-art NallS batteries. As shown in Fig. 3e. Supplementary Figs. 22, 23, and Supplementary Table 7, a comprehensive comparison was conducted among Na||S batteries with sulfur-positive electrodes featuring free of catalytic site^{6,38}, single-atom sites^{23,24,39,40}, metal-particle sites⁴¹⁻⁴⁴, and compound-particle sites⁴⁵⁻⁴⁸. Notably, the Fe-N₁/S positive electrode ranks among the top tier in terms of sulfur utilization, rate performance, and cyclability.

In situ XRD and in situ, EIS measurements were conducted to deeply understand the unsaturated Fe single atom catalyzed sulfur redox. Supplementary Fig. 24 illustrates the variations in peak intensity within the XRD patterns of these positive electrodes throughout cycling. Peaks at 36.8° and 26.6° corresponding to the Na₂S (353) facet and Na₂S₅ (131) facet, were extracted to highlight the differences (Fig. 3f and g). During charging, the Na₂S signal in the Fe–N₁/S positive electrode weakened and nearly disappeared at 3.0 V, while the Na₂S₅ signal gradually increased. In the subsequent discharge process, the Na₂S peak reappears and gradually intensifies, while the Na₂S₅ peak exhibits the opposite trend until it completely disappears at 0.8 V. This indicates that in the Fe-N₁/S positive electrode, sulfur species go through highly reversible conversion, ultimately resulting in the formation of Na₂S as the discharge product. Similar to Fe-N₁/S, changes in the intensity of Na₂S and Na₂S₅ peaks during charge and discharge were also noted for Fe-N₂/S. However, at the end of discharge, a strong Na₂S₅ signal remains, indicating insufficient reduction of long-chain NaPSs. The Fe-N₄/S positive electrode exhibits strong Na₂S signal and weak Na₂S₅ signal throughout the operation, indicating difficulty in Na₂S decomposition. In the NC/S positive electrode, substantial signals of Na₂S and Na₂S₅ persist, indicating significant energy barriers for NaPS conversion due to the absence of Fe-N_x sites. Therefore, Fe-N₁ sites are pivotal in boosting the reactivity of sulfur species and expediting the kinetics of sulfur redox.

Based on in situ electrochemical characterization and spectral data, the sulfur redox process can be elucidated. With regard to the CV curve in Fig. 3a, the R_1/R_2 peaks are indicative of the continuous conversion of long-chain to short-chain NaPSs, while the R_3 peak corresponds to their reduction to Na₂S. During the anodic scan, the O_1 and O_2 peaks signify the oxidation of solid-phase and long-chain NaPSs, respectively. The Fe–N $_1$ /S positive electrode exhibits strong response currents for both long-chain and short-chain NaPSs and minimal polarization, indicating optimal kinetic of sulfur species conversion via Fe–N $_1$ sites.

Additionally, we employed in situ electrochemical impedance spectroscopy (EIS) to monitor the behaviors of sulfur species. The in situ EIS measurements were conducted on Na||S batteries assembled with Fe-N_x/S and NC/S positive electrodes at different states of charge (SoC) for the 2nd cycle at 167.5 mA g⁻¹. As illustrated in Fig. 3h, Supplementary Fig. 25, and Supplementary Tables 8-11, the Fe-N₁/S positive electrode showcased minor changes in ohmic resistance (R_0) and charge transfer resistance (R_{ct}) throughout the entire cycle, indicating that the sulfur species underwent conversion with consistently high efficiency of mass and charge transfer, driven by Fe-N₁ sites. Regarding the Fe-N₂/S positive electrode, a notable increase in R_{ct} occurred at an SoC of ~25%, suggesting gradual generation of the less conductive solid-state product within the positive electrode during discharge. These products can be partially decomposed during charging, as indicated by the decreasing R_{ct} . Comparing the former two electrodes, during the discharge of Na||S batteries with the Fe-N₄/S and NC/S positive electrodes, when SoC ranged from ~50% to 20%, the emergence of additional impedance from the blocking layer at midfrequency in the EIS spectra suggests the accumulation of solid-state products on the positive electrodes surfaces (R_{int}) , hindering further sulfur species conversion⁴⁹. This negative effect was not removed until charge to about ~70% SoC. Owing to the absence of Fe-N_x sites, a larger $R_{\rm int}$ of Na||S batteries with NC/S positive electrodes than that of Fe-N₄/ S positive electrodes can be resolved. In summary, highly unsaturated Fe-N₁ sites are crucial for efficient mass/charge transfer and catalytic conversion during sulfur conversion.

The reversibility and electrochemical stability of Fe–N $_x$ hosts are pivotal for the performance of Na||S batteries. Ex situ XPS was conducted to track valence state changes in the Fe–N $_x$ /S positive electrodes during charge and discharge processes. As shown in Supplementary Fig. 26, the Fe 2p binding energy shifted toward lower values during discharge and fully recovered upon charging, confirming the highly reversible nature of the Fe–N $_x$ sites. Furthermore, HAADF-STEM images of the Fe–N $_x$ /S positive electrode after 700 cycles (Supplementary Fig. 27) reveal that the Fe–N $_x$ sites remain uniformly dispersed without Fe aggregation, underscoring their sustained electrochemical stability. Overall, the high reversibility and electrochemical stability of Fe–N $_x$ hosts underpin the improved electrochemical performance of Na||S batteries.

Based on the redox peak indexes in the CV curves, an in-depth kinetic analysis of each positive electrode was conducted using multirate CV scanning. The varying trends of response current and voltage polarization as functions of scan rate reflect the kinetics of specific sulfur redox steps. As shown in Fig. 4a and Supplementary Fig. 28, the polarization of R₁ in the NC/S and Fe-N₄/S positive electrodes increased rapidly with higher scan rate, since the lack of Fe- N_x sites and the inferior interactions between saturated Fe– N_4 sites and NaPSs. Both Fe-N₂/S and Fe-N₁/S positive electrodes gained higher R₁ currents as the scan rate increased. This phenomenon suggests that unsaturated Fe-N_x sites are susceptible to the conversion of long-chain NaPSs. Regarding the R₃ peak, Fe-N₂/S positive electrodes exhibit low R₃ currents for fewer formation of solid-state NaPSs. Fe–N₁/S positive electrode shows the lowest polarization and highest R₃ currents. In the anodic scan, the O₁ peak is discernible for all of the positive electrodes, while the O₂ peak becomes ambiguous as the scan rate increases.

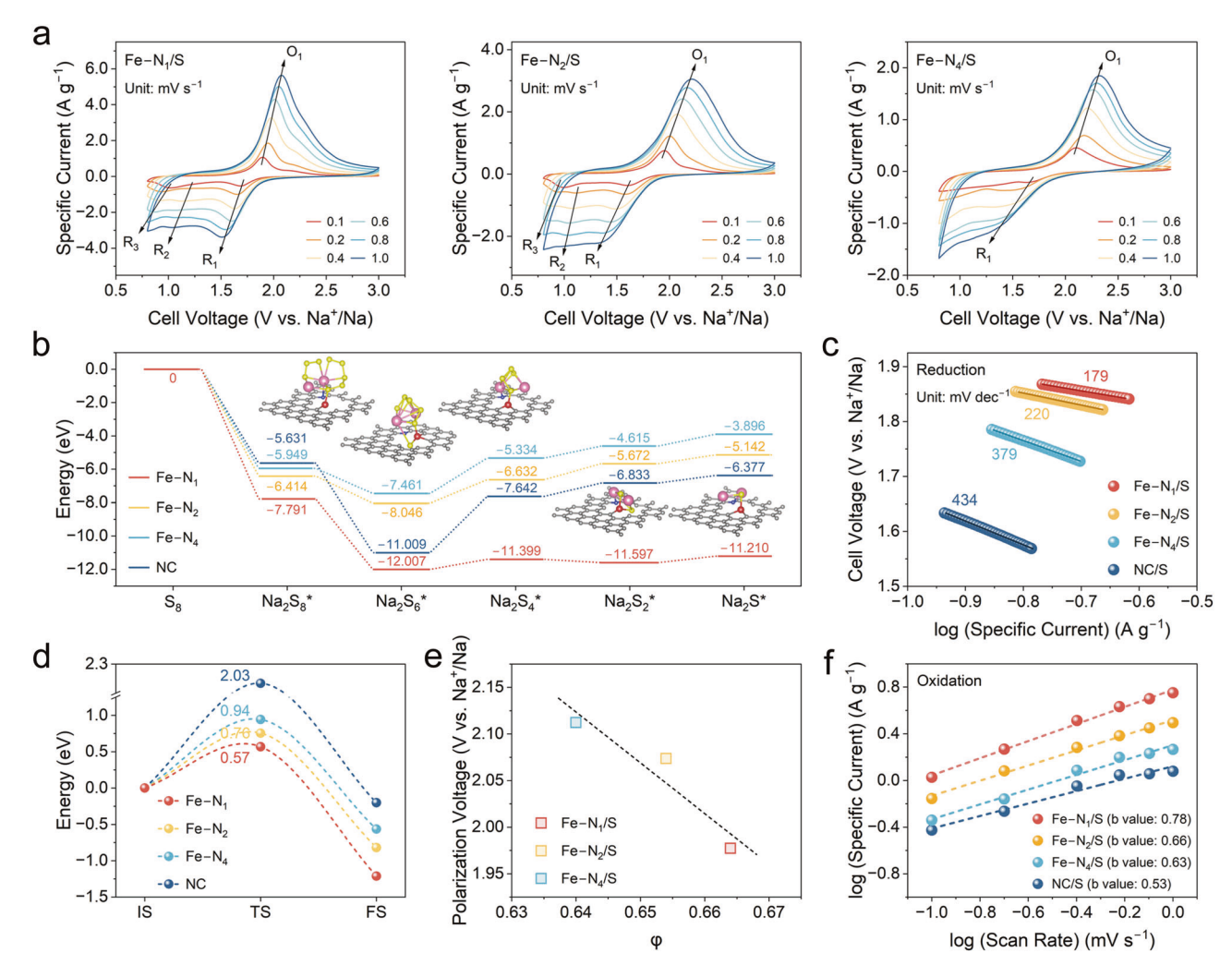


Fig. 4 | The influence of unsaturation degree in Fe-N_x from the electronic structure aspect. a Multi-rate scan CV curves of Na||S batteries with Fe-N₁/S, Fe-N₂/S, and Fe-N₄/S positive electrodes. **b** Gibbs free energy profiles of sulfur reduction processes on Fe-N₁, Fe-N₂, Fe-N₄, and NC hosts. Insets: Corresponding adsorption configuration of sodium polysulfide on Fe-N₁, where the pink, yellow, red, blue, and grey spheres represent Na, S, Fe, N, and C atoms, respectively. **c** Tafel slope of peak R₁ derived from CV curves at 0.2 mV s⁻¹. **d** Energy profiles of the initial

state (IS), transition state (TS), and final state (FS) for Na_2S decomposition on Fe- N_1 , Fe- N_2 , Fe- N_4 , and NC hosts. **e** Relationship between the polarization voltage of O_1 peak at 0.4 mV s⁻¹ and electronic structure descriptor (ϕ) . **f** Linear relationship of log (specific current) vs. log (scan rate) of peak O_1 for the positive electrodes. The atomic coordinates of the configurations are provided as a Supplementary Data 1 file, and source data are provided as a Source Data file.

Compared to the NC/S positive electrode, Fe–N $_x$ /S positive electrodes exhibit higher O $_1$ /O $_2$ currents, indicating improved Na $_2$ S decomposition capabilities from Fe–N $_x$ sites. At high scan rates, the O $_1$ currents of the Fe–N $_1$ /S positive electrode are maximized and the polarization is minimized, suggesting that the increased unsaturation of Fe–N $_x$ sites is closely related to the enhanced Na $_2$ S decomposition capability.

To reveal the origin of sulfur reduction kinetics for these four positive electrodes, the Gibbs free energies along the sulfur reduction pathway were calculated. Per Fig. 4b, among all the sub-steps, the conversion of Na_2S_6 to Na_2S_4 was found to have the highest energy barriers for all positive electrodes, which is identified as the rate-determining step (RDS) for the entire reduction process. The highest RDS energy barrier (3.367 eV) of NC/S accounts for the challenge in converting long-chain to short-chain NaPSs in the absence of Fe- N_x sites. The RDS energy barrier decreases with the increasing unsaturation degree of the Fe- N_x sites. As for the Fe- N_1 sites, the lowest RDS energy barriers ensure their considerable favor in accelerating the kinetics of both long-chain and short-chain NaPSs conversion. To further analyze the role of Fe- N_x sites in the kinetics of sulfur reduction reaction, the R_1 peaks in the CV curves were extracted for fitting the

Tafel slopes. As shown in Fig. 4c, Fe–N $_x$ /S positive electrodes exhibit higher R $_1$ onset potentials and significantly lower Tafel slopes compared to NC/S positive electrodes (434 mV dec $^{-1}$), indicating that Fe–N $_x$ sites can expedite the reduction of NaPSs. The lowest Tafel slope for the Fe–N $_1$ /S positive electrode (179 mV dec $^{-1}$) confirms the advantage of highly unsaturated Fe–N $_1$ sites in catalyzing the long-chain NaPSs reduction.

Furthermore, the CV curves of the Na_2S_8 -, Na_2S_6 -, and Na_2S_4 -based symmetric cells (Supplementary Fig. 29) also verified the optimal catalytic capability of the Fe– N_1 site. We further conducted a quantitative analysis of the symmetric cell data by comparing the redox peak potentials and corresponding currents at various scan rates (Supplementary Fig. 30). Symmetric cells based on Fe– N_1 electrodes consistently displayed the lowest polarization and highest response currents, highlighting the optimal NaPSs redox kinetics enabled by Fe– N_1 sites. Moreover, to elucidate the critical catalytic role of Fe– N_1 in the reduction of solid-phase NaPSs, we conducted Na_2S nucleation tests. As shown in Supplementary Fig. 31, Na_2S nucleation exhibited the earliest onset time and largest capacity on the Fe– N_1 electrode. These results compellingly demonstrate that Fe– N_1 sites can significantly accelerate the nucleation and growth of the Na_2S phase, revealing the

underlying mechanism of the high sulfur utilization of Fe– N_1 /S positive electrodes.

As the initial step in the oxidation process of sulfur species, the decomposition of electrochemically inert Na₂S directly determines the sulfur utilization efficiency in Na||S batteries. Hence, we conducted DFT calculations to determine the energy barriers of Na₂S decomposition on each substrate. As illustrated in Fig. 4d, the energy barriers for the Na₂S decomposition reaction on Fe-N₁, Fe-N₂, Fe-N₄, and NC were calculated to be 0.57, 0.76, 0.94, and 2.03 eV, respectively. This trend is consistent with the ICOHP changes in Fig. 1c. Furthermore, we assessed the correlation between φ and the potentials of O_1 peaks (Fig. 4e). As the φ decreased from 0.664 (Fe–N₁) to 0.640 (Fe–N₄), the polarization voltage of the Na₂S oxidation reaction rose from 1.977 V $(Fe-N_1/S)$ to 2.112 V $(Fe-N_4/S)$. This linear relationship confirms that the electronic structures of the Fe-N_x sites are critical in the decomposition of Na₂S. Descriptor φ can also justify and predict the ability of the coordinatively unsaturated single-atom sites to reduce the Na₂S decomposition energy barriers. To experimentally evaluate the influence of Fe-N_x unsaturation degrees on sulfur redox kinetics, we extracted the b value at the O_1 peak from multi-rate scan CV curves. The b value in equation $i = av^b$ reflects the reaction kinetics (where iand ν represent response current and corresponding scan rate)⁵⁰. The sulfur conversion in Na||S batteries involves a combination of multiple surface-controlled and diffusion-controlled processes, making the b value an effective descriptor for sulfur conversion kinetics (Supplementary Fig. 32). As shown in Fig. 4f, the b values of the O₁ peak for Fe- N_1/S , Fe- N_2/S , Fe- N_4/S , and NC/S positive electrodes are 0.78, 0.66, 0.63, and 0.53, respectively. Fe-N₁/S positive electrodes exhibit the highest b value of the O_1 peak, indicating that it has the greatest advantage in solid-state Na₂S decomposition, which is the essential reason for its enhanced sulfur utilization.

A higher population of Fe– N_x sites available routinely leads to better sulfur conversion kinetics, as comprehensively demonstrated in Supplementary Figs. 33–40 and Supplementary Tables 12, 13 based on control groups of specimens with various Fe– N_x site to sulfur ratios. Of note, in these control groups, the Fe– N_1 site is all identified as possessing the highest catalytic capability towards sulfur conversion.

Geometric structures of the $Fe-N_x$ sites are also important for optimizing the behavior of sulfur species in Na||S electrochemistry. As aforementioned, the geometric structures of unsaturated Fe– N_x sites adjacent to defects are expected to provide NaPSs adsorption spaces and Na⁺ diffusion channels. Therefore, we initially investigated the relationship between the geometric structures of Fe- N_x and the essential Na⁺ diffusion behaviors involved in sulfur redox. The galvanostatic intermittent titration (GITT) technique was employed to investigate the Na⁺ diffusion behavior in various hosts. Notably, Fe-N₁/ S positive electrodes exhibited lower overpotential compared to the other three positive electrodes, indicating more facile reaction kinetics (Fig. 5a). The Na⁺ diffusion coefficient was calculated according to Fick's second law, with results depicted in Fig. 5b. Compared to NC/S positive electrodes, the Na⁺ diffusion coefficient of Fe-N₄/S positive electrodes exists a peak near 1.9 V during discharge, corresponding to the reduction process of long-chain NaPSs. It is suggested that the presence of Fe-N_x sites enhances Na⁺ diffusion in the positive electrodes. However, saturated Fe-N₄ sites exhibit limited catalytic conversion of short-chain NaPSs as revealed by the similar Na⁺ diffusion behavior as NC/S positive electrodes in the subsequent discharge and charge process, leading to frustrated Na2S formation and decomposition. In contrast, both Fe-N₂/S and Fe-N₁/S positive electrodes exhibit high Na⁺ diffusion coefficients at 1.7–2.0 V (discharge), 0.8–1.2 V (discharge), and ca. 2.0 V (charge), indicating the advantage of unsaturated Fe–N_x sites for Na⁺ conduction. Particularly, the defectrich feature of the geometric structures in the Fe-N₁/S positive electrode enables more Na+ transfer to the vicinity of Fe-N1 sites for sulfur redox.

Furthermore, R_{ct} obtained from the multi-temperature EIS spectra was utilized to fit the Arrhenius equation, enabling the determination of the correlation between the thermodynamics of the sulfur species' redox reactions and the kinetics of Na⁺ diffusion at the experimental level^{18,51}. Fig. 5c and Supplementary Figs. 41-44 present the multitemperature EIS spectra of the four positive electrodes in 0.8-3.0 V. Through the linear correlation between 1/T and $\log (1/R_{ct})$, the activation energy (E_a) at a given potential was calculated, as delineated in Fig. 5d. In both the charge and discharge processes, Fe-N₁/S positive electrodes exhibited the lowest activation energy barrier (4.8 and 1.8 kJ mol⁻¹ for sulfur reduction and oxidation reactions, respectively), which was lower than those for Fe-N₂/S, Fe-N₄/S, and NC/S positive electrodes (6.1/4.5, 6.4/12.4, and 12.4/15.8 kJ mol⁻¹, respectively). Combining the calculated Na⁺ diffusion coefficients with the activation energy barriers, Fe-N₁/S positive electrodes possess the highest Na⁺ transfer capacity at the maximum energy barrier, which is attributed to the geometric structures of the highly unsaturated Fe-N₁ sites.

The geometric structures of Fe– N_x are closely associated with the adsorption strength of NaPSs, as indicated by theoretical calculations. Effective immobilization of polysulfides is a prerequisite to inhibit shuttle effects and to facilitate sulfur redox kinetics ^{52,53}. To assess the adsorption capacities of the Fe– N_x sites modified sulfur hosts to polysulfides, Na₂S₆ adsorption experiments were conducted (Fig. 5e). The introduction of Fe– N_x sites enhanced the adsorption capacity of NaPSs informed by the lighter color of Fe– N_x containing solutions compared to NC. Furthermore, all Na₂S₆ species in solution were thoroughly adsorbed by the Fe– N_1 hosts after 12 h, as evidenced by the almost overlapping with the DME solvent in the ultraviolet–visible (UV–vis) spectra. The results of the adsorption experiments match well with the theoretical calculations (Supplementary Fig. 45), based on the correlation between γ and absorbance in Fig. 5f and Supplementary Table 14.

The visual cells serve as suitable measurements to appraise NaPSs conversion kinetics endowed by Fe-N_r sites. As illustrated in Fig. 5g, visual cells were constructed with sodium foil negative electrodes and Fe-N_x/S or NC/S positive electrodes, undergoing 12 h standing and a complete discharge/charge cycle. The dissolved amount of NaPSs in the electrolyte and the condition of the sodium negative electrode surface can reasonably describe the adsorption and conversion kinetics of NaPSs, since the weak adsorption and sluggish conversion of NaPSs supply sufficient time for both their dissolution and shuttling. At the end of the charging process (3.0 V), the counter sodium negative electrode for Fe-N₁/S visual cells remained silvery glow and the electrolyte kept colorless with negligible signals detected in the UV-vis spectrum (Fig. 5h). In addition, the advantages of Fe-N₁ sites in strongly adsorbing and catalytically converting NaPSs are obvious compared to other visual cells, in which massive NaPSs dissolution in electrolytes and conspicuous NaPSs deposition on sodium negative electrodes are observed.

Cycling stability is another important index for evaluating the performance of Na||S batteries. To elucidate the correlation between NaPSs conversion and the cycling stability of Na||S batteries, we collected and examined the positive electrodes (state of charge) after 100 cycles at 1675 mA g $^{-1}$. Figure 6a illustrates that Na₂S₄, Na₂S₄, Na₂S₂, and Na₂S are predominant in post-cycled Fe–N₁/S, Fe–N₂/S, Fe–N₄/S, and NC/S positive electrodes, respectively. Compared to the crystalline Na₂S₄ in Fe–N₂/S positive electrodes, the amorphous products in Fe–N₁/S positive electrodes present favorable electrochemical activities, suggesting that Fe–N₁ sites promote the stability of Na||S batteries. Conversely, the accumulation of electrochemically inert Na₂S/Na₂S₂ in Fe–N₄/S and NC/S positive electrodes results in the loss or even depletion of sulfur species, which is detrimental to the stability.

The morphology and elemental distribution of the post-cycled positive electrodes corroborated the SAED results, as shown in Fig. 6b. The cubic particles in the cycled Fe– N_1 /S positive electrode remain

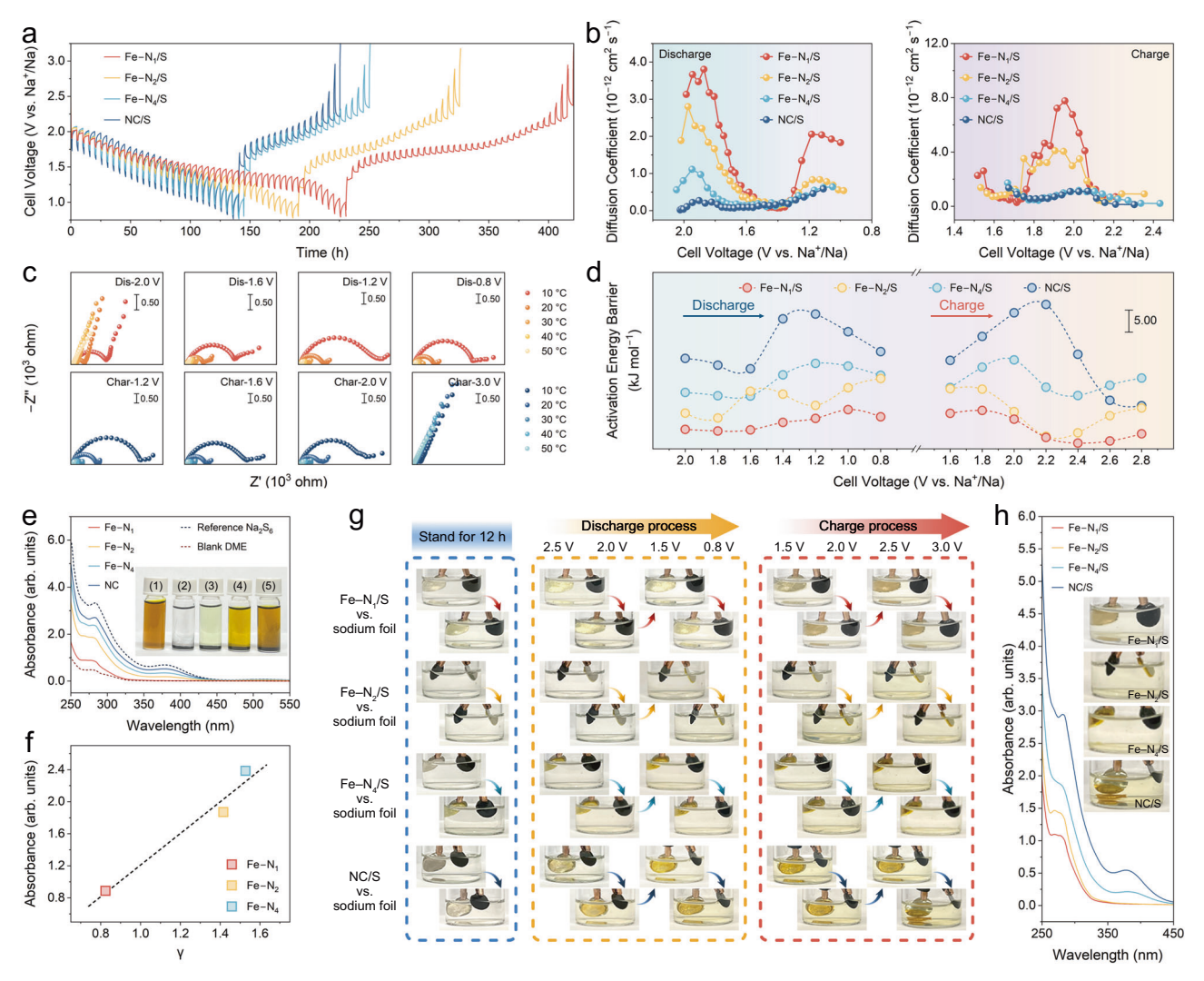


Fig. 5 | **The influence of unsaturation degree in Fe-N**_x **from geometric structure aspect. a** and **b** GITT curves (**a**) and calculated Na⁺ diffusion coefficient (**b**) of Na||S batteries with Fe-N₁/S, Fe-N₂/S, Fe-N₄/S, and NC/S positive electrodes. **c** and **d** Multi-temperature EIS spectra (**c**) and calculated activation energy barriers (**d**) for Na||S batteries with Fe-N₁/S, Fe-N₂/S, Fe-N₄/S, and NC/S positive electrodes. **e** UV-vis spectra and the optical photo of Na₂S₆ solutions with host materials (solutions (1)–(5) in the inset are reference Na₂S₆ solution, and adsorbed solution

with Fe-N₁, Fe-N₂, Fe-N₄, and NC). **f** Relationship between geometric structure descriptor (γ) and absorbance of Na₂S₆ in UV-vis spectra for Fe-N₁, Fe-N₂, and Fe-N₄. **g** Visual cells under different states employing Fe-N₁/S, Fe-N₂/S, Fe-N₄/S, and NC/S positive electrodes. **h** UV-vis spectra and the optical photos visual cells employing different positive electrodes at the end of the charging process. Source data are provided as a Source Data file.

well-defined. The overlap between elemental sulfur distribution and particle morphology suggested effective sulfur species confinement within the composite materials, attributed to the strong adsorption of Fe-N₁ sites. Additionally, the uniform distribution of elemental sodium confirmed the accessibility of Na⁺ within the positive electrodes. Notably, micron-sized secondary particles resulting from extensive NaPSs adhesion were observed in both Fe-N₂/S and Fe-N₄/S positive electrodes. Moreover, the differential distribution of sodium and sulfur indicates the stacking of sodium-rich solid Na₂S/Na₂S₂ and the escaping of sulfur-rich solvable NaPSs. Severe aggregation on cycled NC/S positive electrodes obscured original cubic morphologies. The electrode surface was coated with non-conductive NaPSs, as evidenced by the sulfur distribution exceeding the original morphologies. Due to the lack of catalytic Fe-N_x sites, NC hosts failed to restrain sulfur species migration, resulting in the detachment of the formed products from the hosts.

Based on the above analysis, Supplementary Fig. 46 summarizes the Na \parallel S electrochemical conversion mechanism on Fe–N $_x$ sites with various unsaturation degrees. The NC hosts exhibit poor sulfur redox

kinetics. Sulfur species escape rapidly from micropores, unevenly depositing as Na₂S on the host's surface, blocking pores and impeding mass/charge transfer, leading to the passivation of sulfur species. The saturated Fe-N₄ sites in the Fe-N₄ hosts have weak interactions with NaPSs and insufficient NaPSs redox catalysis. Increasing the unsaturation degree of the Fe-N_x site significantly enhances interactions with sulfur species. The unsaturated Fe-N_x sites with defect-rich configurations reduce the steric-hindrance effect of NaPSs adsorption, allowing for much stronger anchoring of NaPSs by Fe–N_x sites. In terms of electronic structure, unsaturated coordination leaves the central Fe atom with ample hybridization orbitals to couple and interact with NaPSs. As a result of the favorable geometric and electronic structure of Fe-N_x sites, Na||S batteries featuring Fe-N₁/S and Fe-N₂/S positive electrodes demonstrate better electrochemical performances compared to those with Fe-N₄/S positive electrodes. Specifically, Fe-N₁/S positive electrodes exhibit high sulfur utilization and efficient sulfur redox during high-rate and long-term cycling, thereby conferring significant reversible capacity, satisfactory rate performance, and prolonged cycling lifespan to Na||S batteries.

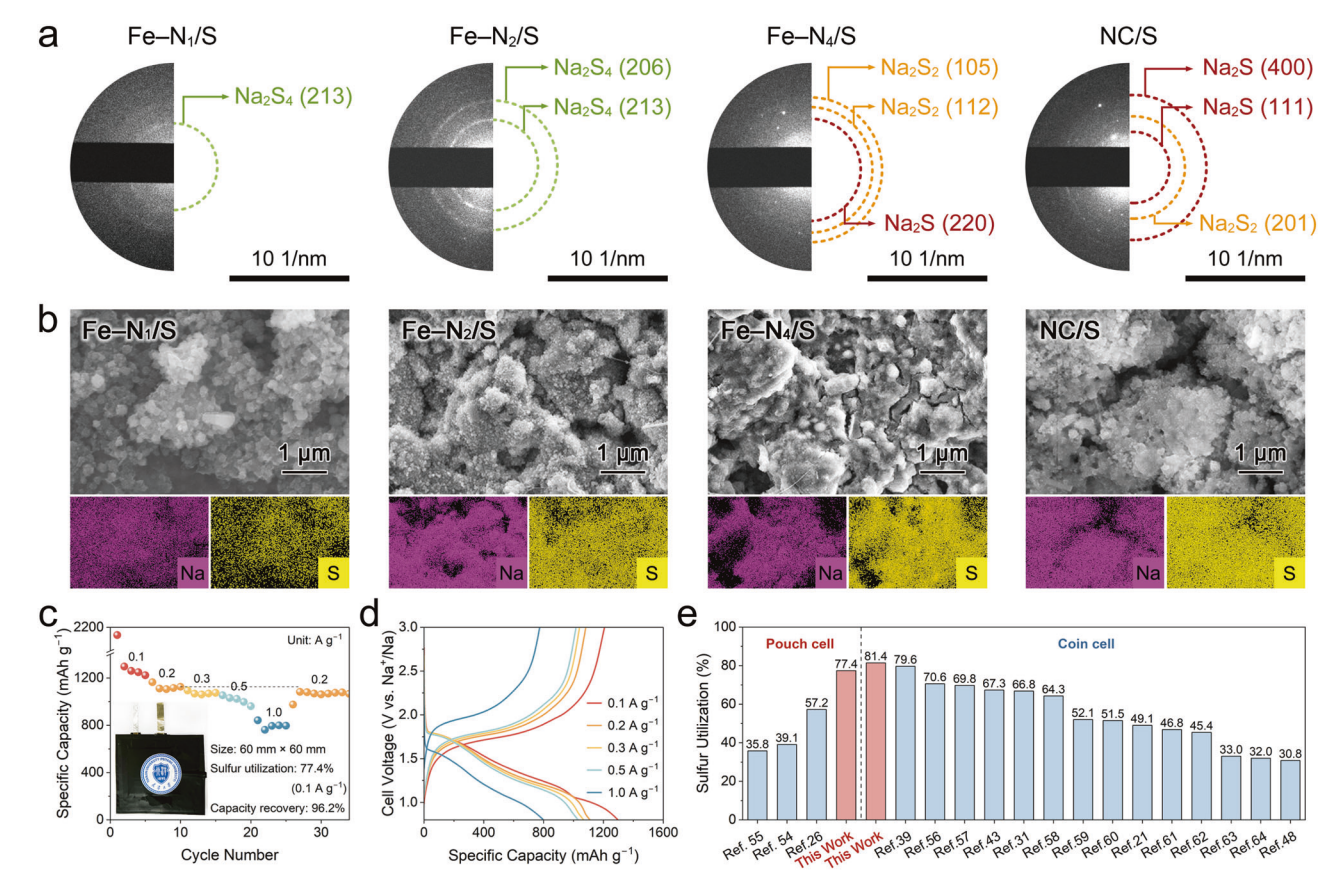


Fig. 6 | Practical application prospect of unsaturated Fe-N_x positive electrodes in Na||S batteries. a and b SAED patterns (a), SEM images, and corresponding EDS mapping (b) of post-cycled Fe-N₁/S, Fe-N₂/S, Fe-N₄/S, and NC/S positive electrodes. c and d Rate performance (c) and corresponding GCD profiles (d) of Na||S

pouch cell employing Fe-N₁/S positive electrode. Inset: Digital image of the assembled Na||S pouch cell configuration. e Sulfur utilization comparison between Fe-N₁/S positive electrode-based Na||S pouch cell and the state-of-the-art Na||S coin cells. Source data are provided as a Source Data file.

To explore the practical application of Fe-N₁/S positive electrodes, Na||S pouch cells (60 × 60 mm²) were assembled. Optical images demonstrated a stable open-circuit voltage (OCV) of 2.32 V under flat and standing conditions (Supplementary Fig. 47), underscoring the adaptability of Na||S batteries to diverse environments. The rate performance and corresponding GCD profiles of the assembled pouch cells are depicted in Fig. 6c and d. Na||S pouch cells employed Fe-N₁/S positive electrodes exhibited reversible capacities of 1296.9, 1124.8, 1073.9, 1030.1, and 799.4 mAh g⁻¹ at different specific currents of 0.1, 0.2, 0.3, 0.5, and 1.0 A g⁻¹, respectively. Notably, specific capacity recovered to 1082.3 mAh g⁻¹ (96.2% of the 10th cycle specific capacity) after switching back to 0.2 A g-1, indicating efficient sulfur utilization of the Fe-N₁/S positive electrode even in pouch cells. Encouragingly, the sulfur utilization of the Fe-N₁/S positive electrode in both Na||S pouch cell and coin cell is improved compared to previous reports (Fig. 6e and Supplementary Tables 15, 16)6,24,26,39,43,48,54-64. In particular, the Na||S pouch cell maintains comparable performance even under low electrolyte conditions of 25 µL mg_{sulfur}⁻¹ (Supplementary Fig. 48). Additionally, visual demonstrations were conducted to validate its practical potential. As shown in Supplementary Fig. 47, two series-connected Nall S pouch cells employing Fe-N₁/S positive electrodes efficiently lighted the light-emitting diode (LED) devices without significant brightness reduction after continuous 20-min operation. Overall, sulfur-positive electrodes based on Fe single atoms with unsaturated coordination exhibit boundless potential for future advanced energy storage devices.

Discussion

In summary, we designed coordinatively unsaturated Fe–N_x (x=1–4) sites modified host materials for sulfur-positive electrodes to optimize

the polysulfide behavior for high-performance Na||S battery. Based on theoretical calculations, geometric structure descriptor γ and electronic structure descriptor φ correlated with the unsaturation degree of Fe– N_x sites were proposed. The negative correlation between γ and the adsorption strength of NaPSs, as well as the positive correlation between φ and the decomposition capability of Na₂S, were established and experimentally verified. The Fe-N₁ sites, theoretically screened and characterized by the lowest γ and the highest φ values, are considered the optimal functional species for sulfur host modification in Na||S batteries. Comprehensive experimental analyses and theoretical calculations indicated that Fe-N1 sites provide sufficient space for NaPSs adsorption. Their electronic structure offers abundant coupling orbitals for solid-phase products, mainly Na₂S, accelerating kinetics and lowering the energy barrier for Na₂S decomposition. As a result, Na||S batteries with Fe-N₁ sites modified positive electrodes exhibit improved sulfur utilization, sustained rate performance, and longterm stability. Additionally, pouch cells using positive electrodes with Fe-N₁ site modification achieved a sulfur utilization of up to 77.4% at a specific current of 0.1 A g⁻¹, comparable to top-level coin cells. This work presents design principles for efficient single-atom-based catalysts for Na||S batteries, providing important guidance for selecting high-performing catalysts and optimizing polysulfide behavior in Na||S batteries.

Methods

Chemicals

Iron(III) acetylacetonate (Fe(acac)₃, 98%), sodium bis(tri-fluoromethanesulfonyl)imide (NaTFSI, 98%), ethylene glycol dimethyl ether (DME, 99.5%), and fluoroethylene carbonate (FEC, 99%) were

purchased from Meryer Chemical Technology Co., Ltd. Zinc nitrate hexahydrate (Zn(NO₃)₂·6H₂O, 99.99%), sodium sulfide (Na₂S, 95%), sodium metal (Na, 99.7%) were purchased from Shanghai Aladdin Biochemical Technology Co., Ltd. 2-Methylimidazole (2-MIM, 98%), hexadecyl trimethyl ammonium bromide (CTAB, 98%), and propylene carbonate (PC, 99%) were purchased from HEOWNS. Sulfur (S, 99.5-100.5%), graphene nanoplatelets, and diethyl carbonate (DEC, 99%) were purchased from Sigma-Aldrich. Methanol (99.9%) and tetra ethylene glycol dimethyl ether (TEGDME, 99%) were purchased from Shanghai Macklin Biochemical Co., Ltd. Carboxymethyl cellulose (CMC, M.W. 250000) was purchased from Shanghai Acmec Biochemical Technology Co., Ltd. N-methyl–2-pyrrolidone (NMP) and poly(vinylidene fluoride) (PVDF) were purchased from Guangdong Canrd New Energy Technology Co., Ltd. All reagents were used directly in the experiments without further purification.

Synthesis of Fe-ZIF-8 and ZIF-8 precursors

In a typical synthesis, $20.0\,\mathrm{mg}$ CTAB, $0.788\,\mathrm{g}$ ($2.65\,\mathrm{mmol}$) $\mathrm{Zn}(\mathrm{NO_3})_2\cdot 6\mathrm{H_2O}$, and $49.4\,\mathrm{mg}$ ($0.14\,\mathrm{mmol}$) $\mathrm{Fe}(\mathrm{acac})_3$ were sequentially dissolved in $28\,\mathrm{ml}$ deionized water to form solution A. $12.97\,\mathrm{g}$ ($0.158\,\mathrm{mol}$) $2\cdot\mathrm{MIM}$ was dissolved in $200\,\mathrm{ml}$ deionized water to form solution B. Afterwards, solution A was slowly poured into solution B and stirred continuously for $24\,\mathrm{h}$. The orange-colored Fe-ZIF-8 powder was collected by centrifugation, washed three times with methanol, and dried in a vacuum oven at $60\,\mathrm{^{\circ}C}$ overnight. The L-Fe-ZIF-8 with low Fe loading was obtained by reducing the amount of Fe(acac) $_3$ introduced to $9.9\,\mathrm{mg}$ ($0.028\,\mathrm{mmol}$) during the synthesis ZIF-8 was obtained without adding Fe sources during the synthesis process.

Synthesis of Fe-N₁ hosts

The L-Fe-ZIF-8 powder was immersed in the N_2 atmosphere and heated up to 1100 °C for 3 h at a heating rate of 5 °C min⁻¹, followed by the furnace cooling to room temperature. The obtained black powders were noted as Fe– N_1 .

Synthesis of Fe-N₂ hosts

The Fe-ZIF-8 powder was treated at 900 °C for 3 h under N_2 gas flow at a heating rate of 5 °C min⁻¹. After cooling to room temperature, the black Fe- N_2 powder was obtained.

Synthesis of Fe-N₄ and NC hosts

The Fe-ZIF-8 and ZIF-8 powders were treated at a rate of 5 $^{\circ}$ C min⁻¹ in an N₂ atmosphere at 700 $^{\circ}$ C for 3 h. The resulting powders were noted as Fe-N₄ and NC, respectively. To enable a more comprehensive comparison, ZIF-8 was pyrolyzed at 900 and 1100 $^{\circ}$ C under identical conditions, yielding products designated as NC (900) and NC (1100).

Synthesis of Fe-N₁/S, Fe-N₂/S, Fe-N₄/S, and NC/S composites

Fe–N $_1$ (or Fe–N $_2$, Fe–N $_4$, NC) host and sulfur were homogeneously mixed at a mass ratio of 1:1, and subsequently vacuum encapsulated in a high boron glass tube. The glass tubes were placed in a muffle furnace and heated up to 155 °C at a heating rate of 5 °C min $^{-1}$ and held for 12 h. After that, the glass tubes were further heated up to 300 °C for an additional 12 h. The composites could be obtained by furnace cooling to room temperature and were denoted as Fe–N $_1$ /S, Fe–N $_2$ /S, Fe–N $_4$ /S, and NC/S. Composites with high sulfur content were prepared using a similar procedure by adjusting the ratio of the Fe–N $_1$ host to sulfur to 4:6 and 3:7, denoted as Fe–N $_1$ /S (60% S) and Fe–N $_1$ /S (70% S), respectively.

Adsorption measurements

The Na₂S₆ solution for adsorption measurements was prepared by mixing Na₂S and sulfur with a molar ratio of 1:5 in DME. 10 mg Fe–N₁,

Fe– N_2 , Fe– N_4 , and NC were added into the 2 ml 0.02 M Na_2S_6 solution, respectively, with the blank Na_2S_6 solution as a reference.

Materials characterization

Scanning electron microscopy (SEM) imaging coupled with an energydispersive X-ray spectrometer (EDS) was conducted using a Jeol JSM-7800F field-emission microscope. Transmission electron microscopy (TEM) characterization, including imaging and selected-area electron diffraction (SAED) pattern acquisition, was carried out on a Jeol JEM-F200 instrument. Atomic-resolution aberration-corrected high-angle annular dark-field scanning transmission electron microscopy (HAADF-STEM) observations were performed on a Jeol JEM-ARM200F system. X-ray photoelectron spectroscopy (XPS) measurements were acquired using a Kratos Axis Supra spectrometer with monochromatic Al Kα excitation. Nitrogen adsorption-desorption isotherms for porosity analysis were recorded on a Micromeritics AutoSorb-IQ gas sorption analyzer. Thermogravimetric analysis (TGA) was performed under a flowing nitrogen atmosphere using a Netzsch STA 449C thermal analyzer. Ultraviolet-visible (UV-vis) absorption spectra were collected with a Shimadzu UV-2700 spectrophotometer equipped with an integrating sphere. In situ X-ray diffraction (XRD) studies were conducted on a Rigaku SmartLab diffractometer operated at 40 kV and 50 mA (Cu K α radiation, λ = 0.15406 nm). The X-ray absorption spectroscopy (XAS) measurements at the Fe K-edge were obtained at beamline BL14W1 of the Shanghai Synchrotron Radiation Facility (SSRF) in transmission mode.

For post-cycling electrode characterization, disassembled electrodes were rinsed repeatedly with DEC solvent to eliminate residual electrolyte salts. After drying, samples were transferred via a vacuum chamber to SEM. Throughout this procedure, the specimens were continuously maintained under an Ar atmosphere or in a vacuum environment to prevent material degradation. Ex-situ characterization followed identical cleaning/drying steps. Electrode materials were scraped, mounted on holders, and sealed in Ar-filled containers. Samples were rapidly transferred to TEM/XPS instruments to minimize air exposure.

Electrochemical measurements

CR2032 coin cells were assembled in an argon-filled glove box with rigorously controlled atmosphere conditions (H₂O < 0.1 ppm, O₂ < 0.1 ppm). The positive electrode slurry was formulated by uniformly blending 70 wt% Fe-N₁/S, Fe-N₂/S, Fe-N₄/S or NC/S composites, 20 wt% graphene nanoplatelets, and 10 wt% CMC with an appropriate amount of deionized water in ambient air using an agate mortar. The slurry was doctor-blade-coated onto carbon-coated aluminum foil at a controlled gap width of 250 µm, followed by overnight vacuum drying at 60 °C. Electrodes were punched into 12 mm disks with a sulfur loading of ca. 1 mg cm⁻². A single sheet of glass fiber separator (GF/C, Whatman; 260 µm thickness, 1.2 µm pore size, 19 mm diameter) was employed. For the sodium metal negative electrode, surface-oxidized layers were mechanically removed from bulk sodium, and 15 mg of fresh sodium was pressed onto a 15.8 mm stainless-steel current collector. The electrolyte (2 M NaTFSI in PC/ FEC, 1:1 v/v) was freshly prepared in the Ar-filled glove box via 12 h stirring at 25 °C prior to assembly. Each coin cell contained 100 μL electrolyte, yielding an electrolyte-to-sulfur (E/S) ratio of ca. $88.5\,\mu L\,mg_{sulfur}^{-1}$ to ensure full separator wetting. Electrochemical characterization was conducted using a NEWARE battery testing system and Solartron multi-channel electrochemical workstation within a 0.8–3.0 V voltage range (vs. Na⁺/Na) in a thermostat at 25 °C. Cycling tests were performed at 167.5, 1675, and 3350 mA g⁻¹, while rate performance was conducted across sequential specific currents of 167.5, 335.0, 502.5, 837.5, 1675, 3350, 5025, 8375, and 167.5 mA g⁻¹. All specific capacities and specific currents were calculated based on the elemental sulfur mass. Coulombic efficiency (CE) was calculated as the ratio of charge-specific capacity to discharge-specific capacity, as follows:

$$CE = \frac{Charge\ capacity}{Discharge\ capacity} \times 100\% \tag{1}$$

CV measurements were carried out on a Solartron multi-channel electrochemical workstation with scanning rates of 0.1-1.0 mV s⁻¹ between 0.8 and 3.0 V. Electrochemical impedance spectroscopy tests were performed at specific voltages in the frequency range 1 MHz-0.01 Hz with an amplitude of 5 mV after resting for 10 min. A thermal test chamber was used to control the temperature during the EIS testing. To stabilize voltage, the batteries were discharged/charged to the specified potential and held at that potential until the output current remained constant. For the pouch cell (6 × 6 cm²), the assembly involved sulfur-positive electrodes with sulfur loading of approximately 1 mg cm⁻² and glass fiber separators. The electrolyte was injected post-sealing via a reserved port, followed by 12 h rest and gas extraction with a syringe before clamping the port. The E/S ratio in low E/S ratio Na||S pouch cell is 25 μL mg_{sulfur}-1. The Na||S pouch cells were cycled under 5 kPa pressure between 0.8 and 3.0 V (vs. Na⁺/Na) using a Solartron multi-channel electrochemical workstation for discharge/ charge measurements. Each data has undergone repeatability testing, mitigating sources of random error through stringent test specifications. The data demonstrates high accuracy and reproducibility, falling within experimental error margins.

Symmetric cell measurements

The Na_2S_6 electrolyte was synthesized by dissolving Na_2S and sulfur (molar ratio corresponds to the nominal stoichiometry of Na_2S_6) in TEGDME containing 2 M NaTFSI, followed by continuous stirring at 60 °C for 24 h to ensure homogeneity. Symmetric cells were assembled using $100\,\mu\text{L}$ of the prepared Na_2S_6 -containing electrolyte (0.052 M) with identical Fe– N_1 , Fe– N_2 , Fe– N_4 , or NC electrodes as both the positive and negative electrodes to investigate polysulfide conversion mechanisms.

Visual cell measurements

For the visual cell tests, the positive electrode slurry was prepared by mixing composites (Fe–N₁/S, Fe–N₂/S, Fe–N₄/S, or NC/S), graphene nanoplatelets, and PVDF at a mass ratio of 7:2:1 in NMP solvent. The resulting slurry was uniformly coated onto carbon paper substrates and dried at 60 °C overnight. Sodium foil pressed onto a stainless-steel collector served as the negative electrode. The electrodes were secured using alligator clips, and the cells were filled with an electrolyte of 2 M NaTFSI in DME. The assembled reaction vessels were sealed and subjected to galvanostatic charge-discharge testing at 167.5 mA g $^{-1}$ using a Solartron multi-channel electrochemical workstation.

Computational methods

Details of the computational methods are provided within the Supplementary Information.

Data availability

All data generated or analyzed during this study are included in the published article. Source data are provided with this paper.

References

- Liu, R. et al. Establishing reaction networks in the 16-electron sulfur reduction reaction. Nature 626, 98 (2024).
- Zhou, G., Chen, H. & Cui, Y. Formulating energy density for designing practical lithium-sulfur batteries. *Nat. Energy* 7, 312 (2022).

- He, J., Bhargav, A., Su, L., Charalambous, H. & Manthiram, A. Intercalation-type catalyst for non-aqueous room temperature sodium-sulfur batteries. Nat. Commun. 14, 6568 (2023).
- Han, Z. et al. Machine-learning-assisted design of a binary descriptor to decipher electronic and structural effects on sulfur reduction kinetics. Nat. Catal. 6, 1073 (2023).
- Zhao, C. et al. A high-energy and long-cycling lithium-sulfur pouch cell via a macroporous catalytic cathode with double-end binding sites. Nat. Nanotechnol. 16, 166 (2021).
- Wu, C. et al. Continuous carbon channels enable full Na-ion accessibility for superior room-temperature Na-S batteries. Adv. Mater. 34, 2108363 (2022).
- Zhou, J. et al. Healable and conductive sulfur iodide for solid-state Li-S batteries. Nature 627, 301 (2024).
- Bhargav, A., He, J., Gupta, A. & Manthiram, A. lithium-sulfur batteries: attaining the critical metrics. *Joule* 4, 285 (2020).
- 9. Kong, L. et al. Current-density dependence of Li₂S/Li₂S₂ growth in lithium-sulfur batteries. *Energy Environ. Sci.* **12**, 2976 (2019).
- Ye, C. et al. The role of electrocatalytic materials for developing post-lithium metal||sulfur batteries. Nat. Commun. 15, 4797 (2024).
- Aslam, M. K. et al. Metal chalcogenide hollow polar bipyramid prisms as efficient sulfur hosts for Na–S batteries. *Nat. Commun.* 11, 5242 (2020).
- Pan, H. et al. Non-encapsulation approach for high-performance Li-S batteries through controlled nucleation and growth. *Nat. Energy* 2, 813 (2017).
- Pang, Q., Liang, X., Kwok, C. Y. & Nazar, L. F. Advances in lithium–sulfur batteries based on multifunctional cathodes and electrolytes. *Nat. Energy* 1, 16132 (2016).
- Manthiram, A., Fu, Y., Chung, S.-H., Zu, C. & Su, Y.-S. Rechargeable lithium-sulfur batteries. Chem. Rev. 114, 11751 (2014).
- Chen, X. et al. Ether-compatible sulfurized polyacrylonitrile cathode with excellent performance enabled by fast kinetics via selenium doping. Nat. Commun. 10, 1021 (2019).
- Ding, J. et al. Review of emerging potassium–sulfur batteries. Adv. Mater. 32, 1908007 (2020).
- 17. Chen, H. et al. Catalytic materials for lithium-sulfur batteries: mechanisms, design strategies and future perspective. *Mater. Today* **52**, 364 (2022).
- 18. Shen, Z. et al. Cation-doped ZnS catalysts for polysulfide conversion in lithium-sulfur batteries. *Nat. Catal.* **5**, 555 (2022).
- Li, H. et al. Developing high-power Li||S batteries via transition metal/carbon nanocomposite electrocatalyst engineering. Nat. Nanotechnol. 19, 792 (2024).
- 20. Yang, X. et al. Cohesive energy discrepancy drives the fabrication of multimetallic atomically dispersed materials for hydrogen evolution reaction. *Nat. Commun.* **15**, 8216 (2024).
- Zhou, S. et al. Visualizing interfacial collective reaction behaviour of Li–S batteries. *Nature* 621, 75 (2023).
- Song, W. et al. Optimizing potassium polysulfides for high performance potassium-sulfur batteries. Nat. Commun. 15, 1005 (2024).
- 23. Lei, Y. et al. Understanding the charge transfer effects of single atoms for boosting the performance of Na-S batteries. *Nat. Commun.* **15**, 3325 (2024).
- 24. Zhang, E. et al. Single-atom yttrium engineering Janus electrode for rechargeable Na–S batteries. *J. Am. Chem. Soc.* **144**, 18995 (2022).
- Zhou, G. et al. Theoretical calculation guided design of single-atom catalysts toward fast kinetic and long-life Li–S batteries. *Nano Lett.* 20, 1252 (2020).
- Bai, R. et al. Toward Complete transformation of sodium polysulfides by regulating the second-shell coordinating environment of atomically dispersed Fe. Angew. Chem. Int. Ed. 62, e202218165 (2023).

- Lim, W.-G. et al. Cooperative electronic structure modulator of Fe single-atom electrocatalyst for high energy and long cycle Li–S pouch cell. Adv. Mater. 35, 2208999 (2023).
- 28. Ding, Y. et al. Enhanced dual-directional sulfur redox *via* a biotemplated single-atomic Fe-N₂ mediator promises durable Li-S batteries. *Adv. Mater.* **34**, 2202256 (2022).
- Huang, Z. et al. Diatomic iron with a pseudo-phthalocyanine coordination environment for highly efficient oxygen reduction over 150,000 Cycles. J. Am. Chem. Soc. 146, 24842 (2024).
- 30. Ruan, J. et al. Linearly interlinked Fe- N_x -Fe single atoms catalyze high-rate sodium-sulfur batteries. *Adv. Mater.* **36**, 2312207 (2024).
- Huang, T. et al. Altering local chemistry of single-atom coordination boosts bidirectional polysulfide conversion of Li–S batteries. Adv. Funct. Mater. 32, 2203902 (2022).
- Peng, L. et al. A fundamental look at electrocatalytic sulfur reduction reaction. Nat. Catal. 3, 762 (2020).
- 33. Ji, X., Lee, K. T. & Nazar, L. F. A highly ordered nanostructured carbon–sulphur cathode for lithium–sulphur batteries. *Nat. Mater.* **8**, 500 (2009).
- Han, Z. et al. Engineering d-p orbital hybridization in single-atom metal-embedded three-dimensional electrodes for Li-S batteries. Adv. Mater. 33, 2105947 (2021).
- 35. Qi, H. et al. Highly selective and robust single-atom catalyst Ru_1/NC for reductive amination of aldehydes/ketones. *Nat. Commun.* **12**, 3295 (2021).
- Zhang, Y. et al. Dual-atoms iron sites boost the kinetics of reversible conversion of polysulfide for high-performance lithium-sulfur batteries. Energy Stor. Mater. 63, 103026 (2023).
- Xu, W. et al. Fundamental mechanistic insights into the catalytic reactions of Li–S redox by Co single-atom electrocatalysts via operando methods. Sci. Adv. 9, eadi5108 (2023).
- Zhang, Y. et al. Chemical and spatial dual-confinement engineering for stable Na–S batteries with approximately 100% capacity retention. Proc. Natl Acad. Sci. USA 120, e2314408120 (2023).
- Jiang, Y. et al. Single-atom vanadium catalyst boosting reaction kinetics of polysulfides in Na–S batteries. Adv. Mater. 35, 2208873 (2022).
- Zhang, B. et al. Atomic cobalt as an efficient electrocatalyst in sulfur cathodes for superior room-temperature sodium-sulfur batteries. Nat. Commun. 9, 4082 (2018).
- Liu, Y. et al. Tungsten nanoparticles accelerate polysulfides conversion: a viable route toward stable room-temperature sodium-sulfur batteries. Adv. Sci. 9, 2105544 (2022).
- Yang, H. et al. Architecting freestanding sulfur cathodes for superior room-temperature Na-S batteries. Adv. Funct. Mater. 31, 2102280 (2021).
- Zhang, S. et al. Mo₂N–W₂N heterostructures embedded in spherical carbon superstructure as highly efficient polysulfide electrocatalysts for stable room-temperature Na–S batteries. *Adv. Mater.* 33, 2103846 (2021).
- Hao, H. et al. Molybdenum carbide electrocatalyst in situ embedded in porous nitrogen-rich carbon nanotubes promotes rapid kinetics in sodium-metal-sulfur batteries. Adv. Mater. 34, 2106572 (2022).
- Qi, Y. et al. A Fe₃N/carbon composite electrocatalyst for effective polysulfides regulation in room-temperature Na–S batteries. *Nat. Commun.* 12, 6347 (2021).
- 46. Wu, J. et al. Bifunctional catalyst for liquid-solid redox conversion in room-temperature sodium-sulfur batteries. *Small Struct.* **3**, 2200020 (2022).
- Ye, H. et al. Amorphous MoS₃ as the sulfur-equivalent cathode material for room-temperature Li–S and Na–S batteries. *Proc. Natl Acad. Sci. USA* 114, 13091 (2017).

- 48. Ye, C. et al. Electron-state confinement of polysulfides for highly stable sodium-sulfur batteries. *Adv. Mater.* **32**, 1907557 (2020).
- Liu, K. et al. N,S-coordinated Co single atomic catalyst boosting adsorption and conversion of lithium polysulfides for lithium-sulfur batteries. Small 18, 2204707 (2022).
- Augustyn, V. et al. High-rate electrochemical energy storage through Li⁺ intercalation pseudocapacitance. *Nat. Mater.* 12, 518 (2013).
- 51. Hua, W. et al. Optimizing the *p* charge of S in *p*-block metal sulfides for sulfur reduction electrocatalysis. *Nat. Catal.* **6**, 174 (2023).
- Zhou, G. et al. Catalytic oxidation of Li₂S on the surface of metal sulfides for Li-S batteries. *Proc. Natl Acad. Sci. USA* 114, 840 (2017).
- 53. Liang, Z. et al. Advances in the development of single-atom catalysts for high-energy-density lithium-sulfur batteries. *Adv. Mater.* **34**, 2200102 (2022).
- 54. Zhang, H. et al. Bidirectional tandem electrocatalysis manipulated sulfur speciation pathway for high-capacity and stable Na-S battery. *Angew. Chem. Int. Ed.* **62**, e202217009 (2023).
- 55. Zhang, H. et al. Atomic manganese manipulating polysulfide speciation pathway for room-temperature Na–S batteries. *CCS Chem.* **6**, 2289–2304 (2024).
- Wang, L. et al. Manipulating the electronic structure of nickel via alloying with iron: Toward high-kinetics sulfur cathode for Na–S batteries. ACS Nano 15, 15218 (2021).
- 57. Li, Z. et al. Room-temperature sodium-sulfur batteries: rules for catalyst selection and electrode design. *Adv. Mater.* **34**, 2204214 (2022).
- 58. Wei, S. et al. A stable room-temperature sodium-sulfur battery. *Nat. Commun.* **7**, 11722 (2016).
- Wang, Y. et al. Tunable electrocatalytic behavior of sodiated MoS₂ active sites toward efficient sulfur redox reactions in roomtemperature Na–S batteries. Adv. Mater. 33, 2100229 (2021).
- 60. Lei, Y. et al. Streamline sulfur redox reactions to achieve efficient room-temperature sodium-sulfur batteries. *Angew. Chem. Int. Ed.* **61**, e202200384 (2022).
- 61. Yan, Z. et al. A high-kinetics sulfur cathode with a highly efficient mechanism for superior room-temperature Na–S batteries. *Adv. Mater.* **32**, 1906700 (2020).
- Yan, Z. et al. Nickel sulfide nanocrystals on nitrogen-doped porous carbon nanotubes with high-efficiency electrocatalysis for roomtemperature sodium-sulfur batteries. *Nat. Commun.* 10, 4793 (2019).
- 63. Wang, Y. et al. Achieving high-performance room-temperature sodium-sulfur batteries with S@interconnected mesoporous carbon hollow nanospheres. *J. Am. Chem.* Soc. **138**, 16576 (2016).
- 64. Ye, C. et al. A Mo_5N_6 electrocatalyst for efficient Na_2S electrodeposition in room-temperature sodium-sulfur batteries. *Nat. Commun.* **12**, 7195 (2021).

Acknowledgements

We acknowledge financial support from the National Natural Science Foundation of China (Nos. 52372218, 52072257, and U22A20119).

Author contributions

W.H. and J.D. conceived the project and designed the experiments. W.S., Z.W., X.W., K.Q., and T.Z. carried out the synthesis and characterization of materials and the electrochemical measurements. W.S. and T.Z. performed the in situ XRD measurements. W.S., H.W., and J.D. performed the DFT calculation. W.S., J.D., and W.H. wrote the paper. All authors discussed the results and commented on the paper.

Competing interests

The authors declare no competing interests.

Additional information

Supplementary information The online version contains supplementary material available at https://doi.org/10.1038/s41467-025-58114-9.

Correspondence and requests for materials should be addressed to Jia Ding.

Peer review information Nature Communications thanks Jinkwang Hwang, who co-reviewed with Di WangShaozhuan Huang for their contribution to the peer review of this work. A peer review file is available.

Reprints and permissions information is available at http://www.nature.com/reprints

Publisher's note Springer Nature remains neutral with regard to jurisdictional claims in published maps and institutional affiliations.

Open Access This article is licensed under a Creative Commons Attribution-NonCommercial-NoDerivatives 4.0 International License, which permits any non-commercial use, sharing, distribution and reproduction in any medium or format, as long as you give appropriate credit to the original author(s) and the source, provide a link to the Creative Commons licence, and indicate if you modified the licensed material. You do not have permission under this licence to share adapted material derived from this article or parts of it. The images or other third party material in this article are included in the article's Creative Commons licence, unless indicated otherwise in a credit line to the material. If material is not included in the article's Creative Commons licence and your intended use is not permitted by statutory regulation or exceeds the permitted use, you will need to obtain permission directly from the copyright holder. To view a copy of this licence, visit http://creativecommons.org/licenses/by-nc-nd/4.0/.

© The Author(s) 2025